

# Ultrahigh mechanical quality factor with Meissner-levitated ferromagnetic microparticles

A. Vinante,<sup>1,2,\*</sup> P. Falferi,<sup>2</sup> G. Gasbarri,<sup>1</sup> A. Setter,<sup>1</sup> C. Timberlake,<sup>1</sup> and H. Ulbricht<sup>1,†</sup>

<sup>1</sup>*School of Physics and Astronomy, University of Southampton, SO17 1BJ, Southampton, UK*

<sup>2</sup>*Istituto di Fotonica e Nanotecnologie - CNR and Fondazione Bruno Kessler, I-38123 Povo, Trento, Italy*

(Dated: June 7, 2022)

We investigate mechanical resonators based on stable Meissner levitation of ferromagnetic microparticles in a cylindrical type-I superconducting trap, and explore the possibility of achieving ultrahigh mechanical quality factors. We are able to detect 5 out of 6 rigid-body mechanical modes, with frequencies in the range 1-400 Hz, using a conventional dc SQUID (Superconducting Quantum Interference Device) with a single pick up coil. The measured frequencies are in substantial agreement with a finite element simulation based on ideal Meissner effect. For two specific modes we find further substantial agreement with analytical predictions based on the image method. We measure damping times exceeding  $10^4$  s and quality factors  $Q$  beyond  $10^7$  which are close to the highest ever measured at low frequencies below 1 kHz. We investigate the possible residual loss mechanisms besides gas collisions, and argue that much longer damping time can be achieved with further effort and optimization. Finally, we discuss a number of applications, including ultrasensitive force and acceleration sensing, magnetometry, fundamental and quantum physics experiments.

Levitated nano/microparticles provide a flexible platform for a wide spectrum of studies, which include cavity optomechanics [1–3], feedback-cooling techniques [4–6], nonlinear dynamics [7], nonequilibrium thermodynamics [8], ultrasensitive force sensing [9, 10] and tests of wave-function collapse models [11–13].

Besides flexibility and tunability of mechanical parameters, a particularly attractive feature of levitated systems is the absence of clamping losses, which are usually a limiting factor in conventional mechanical systems. As a consequence, very low levels of dissipation and decoherence are potentially achievable [14]. Levitation by optical gradient forces is certainly the most popular and developed technique [15]. In spite of remarkable recent results and very high flexibility, optical levitation suffers from relatively high internal temperature, which ultimately leads to thermal noise and decoherence [16].

This suggests that different levitation methods, such as Paul traps [11, 12, 17], or magnetic traps [13, 18–20] could outperform optical levitation in fields in which a low noise level is required, such as force/acceleration sensors or mechanical platforms with ultralow quantum decoherence.

In particular, a new field named quantum magnetomechanics has been envisioned, based on the exploitation of passive magnetic traps and the use of superconducting quantum devices to measure and control the motion on levitated microparticles at very low temperature [16]. This technology would allow testing quantum mechanics in currently inaccessible regimes [21] as well as ultrasensitive force and inertial sensing [19, 22].

In this paper we experimentally demonstrate a simple and effective method to magnetically levitate, trap and

detect individual ferromagnetic microparticles in a type I superconducting trap. We employ hard neodymium alloy ferromagnetic microspheres and a cylindrical lead trap, together with a simple SQUID-based detection. We perform a mechanical characterization at  $T = 4.2$  K at pressures down to  $10^{-5}$  mbar, measuring quality factors in excess of  $10^7$  and damping time in excess of  $10^4$  s. We experimentally investigate the limiting dissipation mechanisms and discuss a number of possible applications, including ultrasensitive force sensing, gravimetry, magnetometry and fundamental and quantum physics experiments.

## I. EXPERIMENTAL SETUP AND MODE IDENTIFICATION

The trap consists of a cylindrical well inside a 99.95%-purity Pb block (Figs. 1a and 1b) with 4 mm diameter and 4 mm depth. The Meissner surface currents induced by the magnetic particle, combined with gravity, provide the vertical confinement, while the lateral surface provides the horizontal one. No special loading procedure is implemented. The magnetic particle is individually manipulated at room temperature and placed at the bottom of the trap before cooling down. Upon cooldown, Meissner repulsion alone is sufficient to overcome electrical surface interaction and levitate the particle. We have checked this behaviour for particle radii down to  $\sim 30$   $\mu\text{m}$ .

We have experimentally demonstrated stable trapping for a variety of spherical and cylindrical magnetic particles with characteristic size in the range  $30 - 1000$   $\mu\text{m}$ . Here, we will focus on the smallest particle we have levitated, a microsphere made of a neodymium-based alloy [23] with radius  $R = (27 \pm 1)$   $\mu\text{m}$  (Fig. 1c), determined by optical microscope inspection. The microsphere has been fully magnetized in a 10 T NMR magnet prior to

\*Electronic address: a.vinante@soton.ac.uk

†Electronic address: h.ulbricht@soton.ac.uk

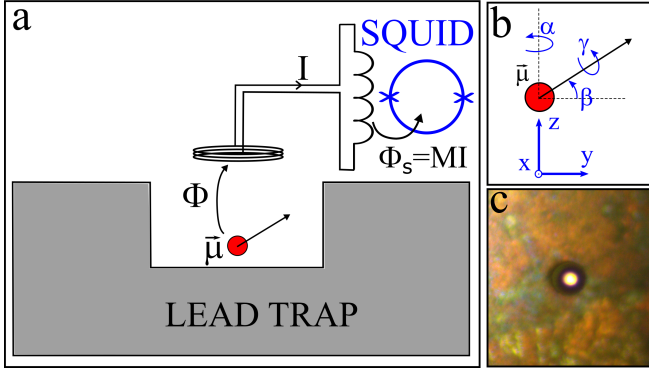


Figure 1: (a) Simplified scheme of the trapping and detection technique. A hard ferromagnetic microparticle is levitated inside a cylindrical well in a type-I superconductor, in our case lead. Meissner repulsion combined with gravity keeps the magnetic particle trapped in all directions. Both the translational and the rotational motion of the particle are detected by a superconducting pick-up connected to a dc SQUID. (b) Conventions adopted on the translational and rotational degrees of freedom. Under weak breaking of cylindrical symmetry, all modes are trapped and detected, except  $\gamma$ . (c) Optical microscope image of a microsphere with radius  $R = (27 \pm 1) \mu\text{m}$  placed on the bottom of the trap. The polycrystalline lead grain boundaries are visible.

the experiment, with an expected saturated magnetization  $\mu_0 M \approx 0.7 \text{ T}$ .

We detect the motion of the particle using a commercial dc SQUID from Quantum Design connected through a single pick-up coil placed above the levitated particle (Fig. 1a). The motion along a given degree of freedom induces a change of the magnetic flux  $\Phi$  in the pick-up coil produced by the permanent magnetic dipole  $\vec{\mu}$  of the particle. As the pick-up coil is connected to the SQUID input coil, this results in a current  $I$  and a flux  $\Phi_S = MI = (M/L) \Phi$  into the SQUID, with  $M$  the mutual inductance between SQUID and input coil. The pick-up coil consists of 6 loops of NbTi wire, wound around a cylindrical PVC holder with radius 1.5 mm, coaxial with the trap. The SQUID is enclosed in a separate superconducting shield. The NbTi wires connecting the SQUID input coil and the pick-up coil are pair-twisted and shielded by a lead tube. We can drive the microparticle by means of a second NbTi coil wound on the same pick-up coil holder, connected to an external resistive line.

Trap and SQUID are enclosed in an indium-sealed vacuum chamber which can be dipped in a standard helium transport dewar. A rough mechanical isolation is obtained by hanging the dewar from the laboratory ceiling through a silicone tube. This reduces seismic noise in the bandwidth 1-20 Hz by more than 1 order of magnitude. A cryoperm shield reduces the earth field by a factor of about 10 at the lead trap location, in order to avoid possible spurious field penetration. After evacuat-

ing the chamber at room temperature, 1 mbar of helium exchange gas is added for thermalization and pumped out after cooldown. We monitor the pressure in the vacuum chamber with a Pirani-Penning gauge placed at room temperature. Pressure data is corrected for the gas composition by assuming that the gas is pure helium.

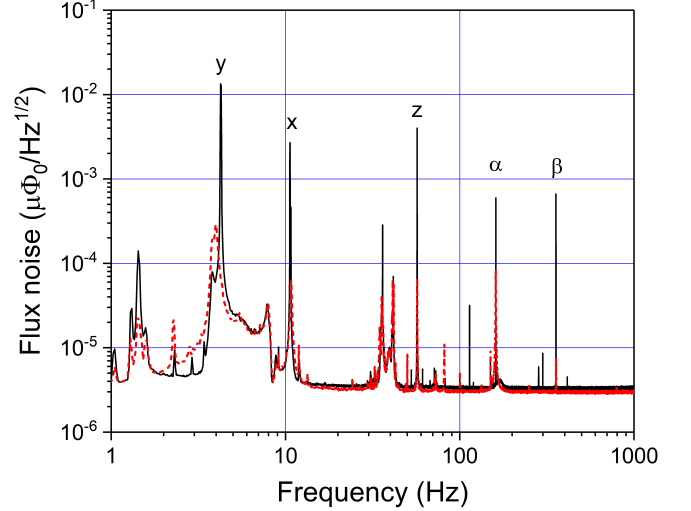


Figure 2: Spectrum of the flux measured by the SQUID at two representative nominal pressures,  $P = 1.6 \times 10^{-5} \text{ mbar}$  (black continuous line) and  $P = 1.0 \times 10^{-2} \text{ mbar}$  (red dotted line). The rigid body mechanical modes of the microsphere are marked by labels.

Fig. 2 shows a typical SQUID spectrum at low and high pressure. Five modes related with the microsphere rigid body motion have been identified, as described below. Other peaks and structures are due to seismic and acoustic noise. We can distinguish the levitated particle modes from spurious peaks thanks to the high quality factor  $Q$  and its characteristic dependence on pressure, as discussed below.

To identify the observed peaks with specific translational and rotational modes of the microparticle, we need a reliable modeling of the system. We parameterize the motion of the particle with the center of mass coordinates  $x, y, z$ , the librational angle  $\beta$  and the azimuthal angle  $\alpha$  defined by the permanent magnetic moment  $\vec{\mu}$ , and the rotation angle  $\gamma$  around  $\vec{\mu}$  (Fig. 1b). The origin is chosen at the center of the bottom surface of the trap. For ideal Meissner effect and trap axis aligned with the gravitational field (i.e. with no tilt), the equilibrium position corresponds to  $x_0, y_0, \beta_0 = 0$  and a finite equilibrium height  $z_0$  depending on the equilibrium between Meissner repulsion and gravity. There will be no confinement in the  $\alpha$  and  $\gamma$  angle, so we would expect to detect only 4 modes. In a real implementation any finite tilt with respect to the Earth gravitational field shifts the horizontal equilibrium position off center, breaking the rotational symmetry around  $\alpha$ , and shifting all frequencies. A trapped  $\alpha$  mode will then show up, leading to 5 detectable modes. Because of symmetry breaking all 5

modes are expected to show some finite coupling to the pick-up coil.

In the following, we will mostly focus on two specific modes, namely the  $z$  and the  $\beta$  ones. Remarkably, the frequency of these modes can be analytically predicted with reasonable accuracy, as a straightforward application of the image method [24, 25]. This is because the dynamics of these modes depends almost exclusively on the interaction of the microsphere with the bottom surface, as long as the equilibrium height  $z_0$  is much smaller than the trap radius. Therefore, the resonance frequency is expected to depend very little on the trap tilt. Indeed, we do observe two modes with relatively stable frequency at  $(56.5 \pm 0.1)$  Hz and  $(377 \pm 5)$  Hz, while the other 3 modes show frequency variations up to 50% upon tilting the experimental setup by a few degrees.

According to the image method [24, 25], the potential energy of a permanent magnet with magnetic moment  $\vec{\mu}$  and mass  $m$ , placed above an horizontal infinite superconducting plane, is given by:

$$U = \frac{\mu_0 \mu^2}{64\pi z^3} (1 + \sin^2 \beta) + mgz \quad (1)$$

Upon minimization one finds that the equilibrium position is achieved at  $\beta = \beta_0 = 0$ , i.e. with the magnet positioned horizontally, and  $z = z_0$ , with:

$$z_0 = \left( \frac{3\mu_0 \mu^2}{64\pi mg} \right)^{\frac{1}{4}} \quad (2)$$

The angular resonance frequencies of the  $z$  and  $\beta$  modes are then easily calculated as  $\omega_z = \sqrt{k_z/m}$  and  $\omega_\beta = \sqrt{k_\beta/I}$ , where  $I$  is the moment of inertia and  $k_z, k_\beta$  are the spring constants:

$$k_z := \left[ \frac{d^2 U}{dz^2} \right]_{(z,\beta)=(z_0,\beta_0)}, \quad (3)$$

$$k_\beta := \left[ \frac{d^2 U}{d\beta^2} \right]_{(z,\beta)=(z_0,\beta_0)} \quad (4)$$

Assuming our particle is a homogeneous sphere, the moment of inertia is  $I = \frac{2}{5}mR^2$  and we finally obtain:

$$\omega_z = \sqrt{\frac{4g}{z_0}} \quad (5)$$

$$\omega_\beta = \sqrt{\frac{5z_0 g}{3R^2}} \quad (6)$$

Interestingly, both frequencies can be written as the square root of the ratio of  $g$  with an effective length, as in a simple pendulum. Furthermore, by multiplying Eq. (5) with Eq. (6) we derive the following remarkable relation:

$$R = \sqrt{\frac{20}{3}} \frac{g}{\omega_z \omega_\beta} \quad (7)$$

which provides the microsphere radius  $R$  as a function of the two frequencies, independent of mass density and magnetization.

Plugging the experimental values of the two stable frequencies into Eq. (7), we obtain a radius  $R = (30.1 \pm 0.5) \mu\text{m}$ , which is 10% higher than the radius  $R = (27 \pm 1) \mu\text{m}$  measured by optical inspection. Further use of Eqs. (5,6) allows identification of the  $z$ -mode at  $\omega_z/2\pi = (56.5 \pm 0.1)$  Hz and the  $\beta$ -mode at  $\omega_\beta/2\pi = (377 \pm 5)$  Hz. The resonance frequencies are correctly reproduced by using the values  $\rho = 7430 \text{ kg/m}^3$  for the mass density and  $\mu_0 M = 0.71 \text{ T}$  for the magnetization, which are consistent with the values provided by the manufacturer. The derived equilibrium height  $z_0 = 311 \mu\text{m}$  is much smaller than the hole radius, which validates the assumption of infinite plane.

A finite element analysis is required to account for the full dynamics and to predict the frequency of all modes. Results from a full 5D finite element simulation of our system based on FEniCS software [26] are shown in Appendix 1. The simulation provides the equilibrium position and the resonant frequencies of all 5 modes, as a function of a finite tilt  $\theta$  up to 3 degrees applied along the  $x$ -axis. The mode frequencies are in reasonable agreement with the experimental results by assuming a tilt of about 3 degrees. In particular, the  $z$  and  $\beta$  mode are in substantial agreement with the image method estimation, and show indeed a weak dependence on the tilt, in contrast with the other modes. The low frequencies peaks in the spectrum (Fig. 2) at about 4 and 10 Hz are identified as the  $y$  and  $x$  mode. The remaining peak is identified as the  $\alpha$  mode. For the latter, a somewhat larger discrepancy between experiment and simulation is observed, with a predicted value of  $\sim 100$  Hz and measured value of about  $\sim 150$  Hz.

The simulation also provides an estimation of the equilibrium values of the 5 independent variables. Assuming the tilt along the  $x$  axis, the equilibrium configuration is  $(x, y, z, \beta, \alpha) \approx (x_0, 0, z_0, 0, \pi/2)$ , with  $z_0$  in agreement within 10% with the image method estimation and  $x_0$  which is strongly dependent on the tilt.

## II. CHARACTERIZATION OF MECHANICAL MODES

We measure the amplitude decay time  $\tau$  of a given mode at frequency  $f = \omega/2\pi$  by means of standard ring-down measurements. The mode is selectively excited at large amplitude by sending a current signal into the excitation coil, and the ringdown is acquired by a lock-in amplifier with reference tuned on the resonance frequency.  $\tau$  is inferred from an exponential fit of the amplitude versus time. The quality factor is calculated as  $Q = \pi f \tau$ . At the lowest measured pressures  $P \sim 10^{-5}$  mbar,  $\tau$  is of the order of several hours and the measurement becomes very difficult, due to the interplay between environmental vibrational noise and the onset of nonlinearities which

restrict the available linear dynamic range. Nevertheless, we could perform reliable ringdown measurements of the  $\beta$  mode at all pressures, and of the  $z$  mode at almost all pressures.

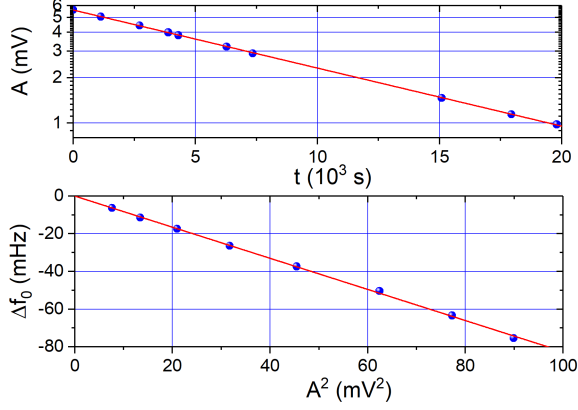


Figure 3: (a) Example of ringdown measurement of the  $\beta$  mode at the lowest nominal pressure  $P = 5.7 \times 10^{-5}$  mbar. (b) Frequency shift of the  $\beta$  mode as a function of the uncalibrated square amplitude, measured during a ringdown.

As first example, we show in Fig. 3a a ringdown measurement of the  $\beta$  mode at nominal pressure  $P = 5.7 \times 10^{-5}$  mbar, featuring a decay time  $\tau = 1.13 \times 10^4$  s and a quality factor  $Q = 1.34 \times 10^7$ . The ringdown is exponential and does not feature significant damping nonlinearities. Instead, we observe a clear spring softening effect, appearing as a negative frequency shift proportional to the square amplitude, as shown in Fig. 3b. This behaviour is entirely expected, as the trapping potential is intrinsically nonlinear. Based on the analytical potential derived from the image method, we can calculate explicitly the expected frequency shift as a function of the angular amplitude (see Appendix 2 for details). This provides an indicative calibration of the absolute value of the angular motion. The absolute motion for the ringdown of the  $\beta$  mode in Fig. 3a corresponds to a range  $\beta = 3 - 20 \times 10^{-3}$  rad, while the typical amplitude of the undriven mode after the exponential ringdown corresponds to about  $10^{-5}$  rad. This is comparable with the mean thermal motion, which can be estimated as  $\beta_{th} = \sqrt{k_B T / k_\beta} \approx 6 \times 10^{-6}$  rad, suggesting that the  $\beta$  mode is close to a thermal noise limited regime.

In Figs. 4a and 4b we show a similar ringdown and frequency shift measurement of the mode  $z$ . The ringdown is acquired at nominal pressure  $P = 1.0 \times 10^{-4}$  mbar, and shows a decay time  $\tau = 1.17 \times 10^4$  s and a quality factor  $Q = 2.1 \times 10^6$ . The frequency shift measurement shows a behaviour similar to the  $\beta$  mode, proportional to the square of the oscillation amplitude. Using the expected frequency shift from the image method, we find that the absolute motion in the ringdown measurement corresponds to a range  $z = 10 - 20 \mu\text{m}$ , while the typical amplitude of the undriven mode corresponds to

about  $0.2 \mu\text{m}$ . In contrast with the  $\beta$  mode, the motion of the undriven mode is much larger than the expected mean thermal motion  $z_{th} = \sqrt{k_B T / k_z} \approx 0.7$  nm. This suggests that the  $z$  mode is dominated by excess environmental disturbance, likely seismic noise. A further mechanical isolation by at least 3 orders of magnitude would be needed to suppress excess noise well below the thermal noise.

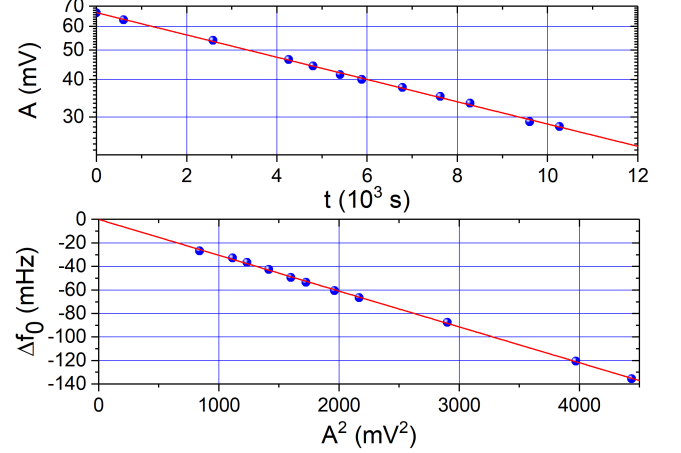


Figure 4: (a) Ringdown measurement of the  $z$  mode at the nominal pressure  $P = 1 \times 10^{-4}$  mbar. (b) Frequency shift of the  $z$  mode as a function of the uncalibrated square amplitude, measured during a ringdown.

Let us discuss the behaviour of damping as a function of the gas pressure. For high pressure,  $P > 10^{-4}$  mbar, we find very similar  $\tau$  for all 5 modes, regardless of frequency. This is in agreement with standard gas damping models, which predict for translational and rotational (amplitude) damping in molecular regime the following expressions [27, 28]:

$$\frac{1}{\tau_t} = \frac{1}{2} \left( 1 + \frac{8}{\pi} \right) \frac{P}{\rho R v_{th}} \quad (8)$$

$$\frac{1}{\tau_r} = \frac{5}{\pi} \frac{P}{\rho R v_{th}} \quad (9)$$

where  $P$  is the gas pressure,  $v_{th} = \sqrt{8k_B T / \pi m_g}$  the mean velocity of the gas molecules, with  $m_g$  gas molecular mass, and  $\rho$  and  $R$  density and radius of the microsphere. The two expressions are indeed frequency-independent, depend linearly on pressure and differ from each other by  $\sim 10\%$ .

Subsequently, we have measured  $\tau$  for the  $z$  and  $\beta$  modes at several pressures. The data is shown in Fig. 5. In order to compare the data with the gas damping model, we have to identify the pressure  $P$  in Eqs. (8,9) with the pressure  $P_c$  of the gas in the cold side of the vacuum chamber at  $T_c = 4.2$  K, where the microparticle is levitated. In general,  $P_c$  differs from the nominal pressure  $P_w$  measured by the pressure gauge at the warm side (room) temperature  $T_w$ , due to the so called thermomolecular effect [29]. This phenomenon was studied in

detail for the case of helium gas between 4 K and 300 K by Weber and Schmidt [30, 31] and interpolating formulae are reported in Ref. [29]. In Fig. 5 the pressure on the  $x$ -axis is the cold pressure  $P_c$  obtained from the Weber-Schmidt model by specifying the measured warm pressure  $P_w$  and the inner radius  $r = 0.97$  cm of the stainless steel tube which connects the cold chamber to the warm gauge pressure. In the limit of low pressure, the thermomolecular pressure ratio scales as  $P_c/P_w = (T_c/T_w)^{1/2}$  and becomes independent of geometric factors.

The data for both the  $\beta$  mode and the  $z$  modes in Fig. 5 are fitted by a second-order polynomial fit significantly better than by a linear fit. We attribute the deviation from the expected linear behaviour to an imperfect estimation of  $P_c$ . The Weber-Schmidt formulae are obtained for ideal cylindrical connecting tubes, but in our experiment this is a crude approximation, due to the presence of the wiring inside the tube. However, as the low pressure limit of Weber-Schmidt formulae is independent of form factors of the connecting tube, we expect Eqs. (8,9) to be valid in this limit. Indeed, the linear terms obtained from the fits are respectively  $(5.6 \pm 0.3) \text{ s}^{-1}/\text{mbar}$  for the  $\beta$  mode and  $(6.2 \pm 0.5) \text{ s}^{-1}/\text{mbar}$  for the  $z$  mode. These estimations are in good agreement with the theoretical predictions  $5.35 \text{ s}^{-1}/\text{mbar}$  and  $5.96 \text{ s}^{-1}/\text{mbar}$  obtained from Eqs. (8,9), using the measured values of  $R$  and the nominal density of the material  $\rho = 7430 \text{ kg/m}^3$  provided by the manufacturer. The agreement provides an indirect support to the Weber-Schmidt model. A notable feature of the gas damping model which is reproduced by the experiment is the ratio of translational to rotational damping of the order of 1.1.

For the  $\beta$  mode the intercept of the fit  $1/\tau_{\beta 0} = (4.3 \pm 0.2) \times 10^{-5} \text{ s}^{-1}$  corresponds to a quality factor  $Q = 2.7 \times 10^7$  at vanishing gas pressure. For the  $z$  mode the intercept of the fit  $1/\tau_{z 0} = (-5 \pm 6) \times 10^{-6} \text{ s}^{-1}$  is instead compatible with zero. This suggests that the residual damping time of the  $z$  mode is longer than 1 day, while the  $Q$  factor may be of the same order of that of the  $\beta$  mode at some  $10^7$ .

### III. DISCUSSION

While higher quality factors have been reported in several systems, both in optically levitated nanoparticles and in clamped overstressed membranes, values exceeding  $10^7$  are not easily obtained. At frequency below 1 kHz, comparable or higher  $Q$  factors are observed only in much more massive systems, such as the pendulums employed by gravitational wave detectors, where dissipation dilution is pushed to the extreme limits [32]. Compared to previous attempts of magnetically levitating a ferromagnetic particle above a superconductor [19, 20] we obtain quality factors 3 orders of magnitude higher.

The comparison between  $\beta$  mode and  $z$  mode suggests that when the pressure is reduced towards 0 the dissipation moves from a gas damping regime, where the damp-

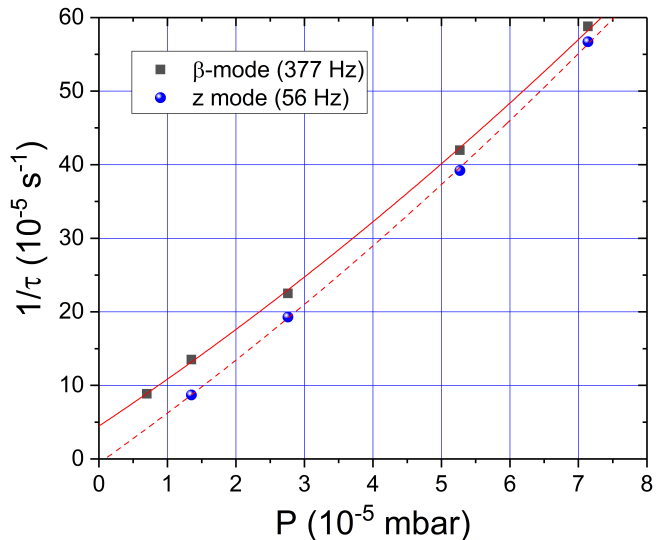


Figure 5: Measured amplitude damping time as a function of the effective pressure at  $T = 4.2$  K calculated using the Weber-Schmidt model. The data refer to the  $\beta$  mode (black squares) and  $z$  mode (red circles). Solid and dashed lines are second order polynomial fits to the  $\beta$  and  $z$  mode data.

ing  $1/\tau$  is independent of frequency, to a regime in which  $1/\tau$  grows with frequency. This may correspond for instance to a loss angle  $1/Q$  either constant or increasing with frequency. Under this regime the modes at low frequency should then achieve a  $Q$  of the order of  $10^7$  or higher. For a mode at 3–4 Hz, as the  $y$  mode in the present experiment, this would translate to a damping time  $\tau \approx 1$  month.

Besides the obvious damping related with the gas, which can be in principle reduced to negligible levels by operating at lower pressure and temperature, we still need to discuss the origin of the residual dissipation, which is apparent at least in the  $\beta$  mode data. We consider magnetic and eddy current losses in the ferromagnetic sphere and losses in the superconductor as possible options.

Estimations of the first two sources are reported in Appendix 3. For our particle, the order of magnitude of eddy current losses is  $Q \approx 10^{10}$ , so we can reasonably rule them out as the dominant effect. On the other hand magnetic hysteresis losses in the ferromagnetic particle could give the right order of magnitude, assuming a magnetic susceptibility with imaginary part of order  $10^{-3}$ .

A hint on the limiting loss mechanism could be given by the dependence of the  $Q$  factor on the microparticle size. We have performed additional measurements on a second similar particle with radius  $a = 39 \mu\text{m}$  finding a residual  $Q = 6 \times 10^6$  for the  $\beta$  mode. Other measurements performed with a different type of magnetic particle, such as cylinders with size larger of  $200 \times 400 \mu\text{m}$  have shown  $Q$  factors below  $10^6$ . The general trend is therefore towards an improvement of  $Q$  by lowering the particle size. As shown in Appendix 3, magnetic losses in the particle are

in principle consistent with this picture.

Finally let us consider possible effects arising from non-idealities in the superconducting lead trap. Under ideal Meissner effect we do not expect significant losses from the superconductor, due to oscillation frequency being many orders of magnitude smaller than the superconducting gap frequency [22]. However, it is notoriously difficult to observe ideal Meissner effect in real type-I superconducting samples [33]. Flux penetration and mixed states can arise even in very pure lead polycrystalline samples. Normal metal regions arising from partial field penetration may in principle cause additional eddy current dissipation [20].

In order to investigate a possible role of flux penetration in our experiment, we have performed additional measurements by applying an external field to the lead trap during the superconducting transition. The field is applied through a superconducting coil placed outside the lead trap. Flux penetration appears as a shift of the  $z$  and  $\beta$  modes with respect to the typical values obtained in absence of applied field. We find that flux penetration shows up at fields down to  $50 \mu\text{T}$ , much lower than the nominal critical field of lead  $H_c = 80 \text{ mT}$ , and comparable with the Earth magnetic field. The amount of flux penetration and frequency shift is not reproducible upon thermal cycling of the superconductor. For large frequency shifts, above 20%, we also observe a strong increase of dissipation, up to 2-3 orders of magnitude. This finding indicates that a strong attenuation of any external field is crucial to achieve high  $Q$ . In our experiment the magnetic shielding reduces the Earth field to the level of a few  $\mu\text{T}$ . This is one order of magnitude lower than the field necessary to cause significant flux penetration, indicating that residual losses due to flux penetration are likely negligible in the current setup.

An interesting conclusion is that our experimental technique can be used to probe deviations from the ideal Meissner effect in a macroscopic sample of a type I superconductor, and to assess the conditions under which ideal Meissner effect can effectively show up.

#### IV. OUTLOOK AND POSSIBLE APPLICATIONS

In this section we discuss a number of possible applications of magnetically levitated ferromagnetic microparticles with ultralow damping.

The most direct use is as ultrasensitive force sensors. For a thermal noise limited operation in the low pressure limit at  $T = 4.2 \text{ K}$ , the microparticle described in this work would feature a force noise spectral density  $S_f = 4k_B T m \omega_0 / Q \approx 1 \text{ aN}/\sqrt{\text{Hz}}$  for the  $z$  mode, assuming a frequency independent residual  $Q$  of  $3 \times 10^7$ . For a very low frequency mode at  $1 \text{ Hz}$  and operation at  $100 \text{ mK}$  the noise would drop to  $0.03 \text{ aN}/\sqrt{\text{Hz}}$ . These figures can be currently achieved only with much smaller masses, such as carbon nanotubes [34] or optically lev-

itated nanoparticles [9] with diameter below  $100 \text{ nm}$ . However, if the force to be measured scales with size of the particle, such as in the case of gravitational or magnetic forces, the signal to noise ratio for our magnetic microparticle would be dramatically better.

Potential use as subresonant wideband gravimeter can be considered. Indeed, for operation at  $T = 4.2 \text{ K}$  and a lowest mode at  $1 \text{ Hz}$  with  $Q = 3 \times 10^7$ , we estimate a thermal noise limited acceleration noise of  $3 \times 10^{-10} \text{ m/s}^2/\sqrt{\text{Hz}}$ , which would be competitive with the best known gravimeters [35] despite the much smaller size. Due to the compactness of our setup, an attractive possibility is the realization of gravity gradiometers composed of several pairs of identical trapped particles [36]. A specific design optimized to suppress frequency drifts will be needed to realize practical devices. Moreover, feedback cooling of all normal modes is technically required to avoid nonlinear effects.

Levitated ferromagnetic particles have been recently proposed as ultrasensitive magnetometers [37]. We can use our particle to detect ultralow magnetic fields by exploiting the sensitivity of rotational modes to small torques. For the  $\beta$  mode at the thermal noise limit we estimate a torque noise  $\sqrt{S_T} = 7 \times 10^{-23} \text{ Nm}/\sqrt{\text{Hz}}$ . If we consider a  $B$  field along the  $z$  axis applied around the resonance frequency  $\omega_\beta$ , the modulus of the torque will be  $T = \mu B$  which implies a magnetic field spectral density  $S_B \approx 1.1 \times 10^{-15} \text{ T}/\sqrt{\text{Hz}}$ . This figure is comparable with the best known SQUID-based [38] or atomic [39] magnetometers with characteristic size of several mm. Therefore, despite being sensitive only on a narrow band around resonance, our levitated particle appears to even outperform existing state-of-the-art magnetometers in terms of field resolution normalized over the sensed magnetic field volume. This feature suggests a possible use to probe exotic spin-dependent interactions of electrons [37] or to look for exotic interactions mediated by axion-like particles [40].

Other applications can be envisioned in the context of fundamental and quantum physics. Ultralow damping  $1/\tau$  and temperature are key ingredients to perform strong noninterferometric tests of wavefunction collapse models [41, 42]. Our fully passive levitation technique offers the unique option of combining ultralow damping with the operation at very low temperature. Ultralow damping alone can be used to set significant bounds on so called dissipative extensions of collapse models [12]. Another possible development is to spin the particle to high speed in a free rotational mode. A fast spinning conductive particle could be used to probe Zeldovich superradiance [43], an effect fully equivalent to the Penrose process of particle creation in a rotating black hole.

Finally, we mention the potential use of ultrasensitive magnetically levitated particles for even more ambitious experiments, such as measuring the gravitational constant  $G$  with small test masses [44], fundamental direct tests of the quantum superposition principle and gravitationally induced collapse [21], gravity-induced entangle-



ment and tabletop tests of quantum gravity [45, 46].

### Acknowledgments

We thank V. Sglavo, G. Guella, P. Connell and M. Utz for technical help. We acknowledge financial sup-

port from the EU H2020 FET project TEQ (Grant No. 766900), the Leverhulme Trust (RPG-2016-046), the COST Action QTSpace (CA15220), INFN and the Foundational Questions Institute (FQXi).

- 
- [1] N. Kiesel, F. Blaser, U. Delic, D. Grass, R. Kaltenbaek, and M. Aspelmeyer, *Cavity cooling of an optically levitated submicron particle*, PNAS 110, 14180 (2013).
  - [2] D. Windey, C. Gonzalez-Ballester, P. Maurer, L. Novotny, O. Romero-Isart, R. Reimann, *Cavity-based 3D cooling of a levitated nanoparticle via coherent scattering*, Phys. Rev. Lett. 122, 123601 (2019).
  - [3] U. Delić, M. Reisenbauer, D. Grass, N. Kiesel, V. Vuletić, M. Aspelmeyer, *Cavity cooling of a levitated nanosphere by coherent scattering*, Phys. Rev. Lett. 122, 123602 (2019).
  - [4] T. Li, S. Kheifets, and M.G. Raizen, *Millikelvin cooling of an optically trapped microsphere in vacuum*, Nature Phys. 7 527-530 (2011).
  - [5] J. Gieseler, B. Deutsch, R. Quidant, and L. Novotny, *Subkelvin Parametric Feedback Cooling of a Laser-Trapped Nanoparticle*, Phys. Rev. Lett. 109, 103603 (2012).
  - [6] J. Vovrosh, M. Rashid, D. Hempston, J. Bateman, M. Paternostro, and H. Ulbricht, *Parametric feedback cooling of levitated optomechanics in a parabolic mirror trap*, J. Opt. Soc. Am. B 34, 1421 (2017).
  - [7] J. Gieseler, L. Novotny, R. Quidant, *Thermal nonlinearities in a nanomechanical oscillator*, Nature Phys. 9, 806 (2013).
  - [8] J. Gieseler, R. Quidant, C. Dellago, L. Novotny, *Dynamic relaxation of a levitated nanoparticle from a non-equilibrium steady state*, Nature Phys. 9, 358 (2014).
  - [9] D. Hempston, J. Vovrosh, M. Toroš, G. Winstone, M. Rashid, H. Ulbricht, *Force sensing with an optically levitated charged nanoparticle*, Appl. Phys. Lett. 111, 133111 (2017).
  - [10] M. Rashid, M. Toroš, A. Setter, H. Ulbricht, *Precession Motion in Levitated Optomechanics*, Phys. Rev. Lett. 121, 253601 (2018).
  - [11] A. Vinante, A. Pontin, M. Rashid, M. Toroš, P.F. Barker, H. Ulbricht, *Testing collapse models with levitated nanoparticles: Detection challenge*, Phys. Rev. A 100, 012119(2019).
  - [12] A. Pontin, N.P. Bullier, M. Toroš, P.F. Barker, *An ultra-narrow line width levitated nano-oscillator for testing dissipative wavefunction collapse*, arXiv:1907.06046.
  - [13] D. Zheng et al, *Room temperature test of wavefunction collapse using a levitated microoscillator*, arXiv:1907.06896.
  - [14] D.E. Chang, C.A. Regal, S.B. Papp, D.J. Wilson, J. Yeb, O. Painter, H.J. Kimble, and P. Zoller, *Cavity optomechanics using an optically levitated nanosphere*, PNAS 107, 1005 (2010).
  - [15] A. Ashkin, J.M. Dziedzic, J.E. Bjorkholm, and S. Chu, *Observation of a single-beam gradient force optical trap for dielectric particles*, Opt. Letters 11, 288 (1986).
  - [16] O. Romero-Isart, L. Clemente, C. Navau, A. Sanchez, and J. I. Cirac, *Quantum Magnetomechanics with Levitating Superconducting Microspheres*, Phys. Rev. Lett. 109, 147205 (2012).
  - [17] W. Paul, *Electromagnetic traps for charged and neutral particles*, Rev. Mod. Phys. 62, 531 (1990).
  - [18] B.R. Slezak, C.W. Lewandowski, J-F. Hsu and B. D’Urso, *Cooling the motion of a silica microsphere in a magneto-gravitational trap in ultra-high vacuum*, New J. Phys. 20, 063028, (2018).
  - [19] C. Timberlake, G. Gasbarri, A. Vinante, A. Setter, H. Ulbricht, *Acceleration sensing with magnetically levitated oscillators*, Appl. Phys. Lett. 115, 224101 (2019).
  - [20] T. Wang, S. Lourette, S.R. O’Kelley, M. Kayci, Y.B. Band, D.F. Jackson Kimball, A.O. Sushkov, and D. Budker, *Dynamics of a Ferromagnetic Particle Levitated over a Superconductor*, Phys. Rev. Applied 11, 044041 (2019).
  - [21] H. Pino, J. Prat-Camps, K. Sinha, B. P. Venkatesh, and O. Romero-Isart, *On-chip quantum interference of a superconducting microsphere*, Quant. Sci. Techn. 3, 025001(2018).
  - [22] J. Prat-Camps, C. Teo, C.C. Rusconi, W. Wiecezorek, and O. Romero-Isart, *Ultrasensitive Inertial and Force Sensors with Diamagnetically Levitated Magnets*, Phys. Rev. Appl. 8, 034002 (2017).
  - [23] Magnequench, MQP-S-11-9-20001 isotropic powder, URL <https://mqtechnology.com/>
  - [24] J.D. Jackson, *Classical Electrodynamics*, 3rd ed. Wiley, New York, 1998.
  - [25] Q.G. Lin, *Theoretical development of the image method for a general magnetic source in the presence of a superconducting sphere or a long superconducting cylinder*, Phys. Rev. B 74, 024510 (2006).
  - [26] M.S. Alnæs, J. Blechta, J. Hake, A. Johansson, B. Kehlet, A. Logg, C. Richardson, J. Ring, M.E. Rognes, and G.N. Wells, *The FEniCS Project Version 1.5*, Arch. Numer. Software 3, 9 (2015).
  - [27] P.S. Epstein, *On resistance experienced by spheres in their motion through gases*, Phys. Rev. 23, 710 (1924).
  - [28] A. Cavalleri, G. Ciani, R. Dolesi, M. Hueller, D. Nicolodi, D. Tombolato, S. Vitale, P.J. Wass, W.J. Weber, *Gas damping force noise on a macroscopic test body in an infinite gas reservoir*, Phys. Lett. A 374, 3365 (2010).
  - [29] T.R. Roberts and S.G. Sydorik, *Thermomolecular Pressure Ratios for He<sup>3</sup> and He<sup>4</sup>*, Phys. Rev. 102, 304 (1956).
  - [30] S. Weber, Leiden Comm. No. 264b (1936); 264d (1936); and Suppl. 71b (1932).
  - [31] S. Weber and G. Schmidt, Leiden Comm. No 246c (1936).
  - [32] P. Willems, V. Sannibale, J. Weel, V. Mitrofanov, *Investigations of the dynamics and mechanical dissipation of a fused silica suspension*, Phys. Lett. A 297, 37 (2002).
  - [33] W. Treimer, O. Ebrahimi, and N. Karakas, *Observation of partial Meissner effect and flux pinning in supercon-*

- ducting lead containing non-superconducting parts, Appl. Phys. Lett. 101, 162603 (2012).
- [34] J. Moser, J. Güttinger, A. Eichler, M.J. Esplandiu, D.E. Liu, M.I. Dykman, A. Bachtold, *Ultrasensitive force detection with a nanotube mechanical resonator*, Nature Nanotechnology 8, 493 (2013).
  - [35] John. M. Goodkind, *The superconducting gravimeter*, Rev. Sci. Instrum. 70, 4131 (1999).
  - [36] C.E. Griggs, M.V. Moody, R.S. Norton, H.J. Paik, and K. Venkateswara, *Sensitive Superconducting Gravity Gradiometer Constructed with Levitated Test Masses*, Phys. Rev. Appl. 8, 064024 (2017).
  - [37] D.F. Jackson Kimball, A.O. Sushkov, and Dmitry Budker, *Precessing Ferromagnetic Needle Magnetometer*, Phys. Rev. Lett. 116, 190801 (2016).
  - [38] M. Schmelz, R. Stolz, V. Zakosarenko, T. Schönau, S. Anders, L. Fritzsche, M. Mück, M. Meyer, H.-G. Meyer, *Sub-fT/Hz<sup>1/2</sup> resolution and field-stable SQUID magnetometer based on low parasitic capacitance sub-micrometer cross-type Josephson tunnel junctions*, Physica C: Superconductivity and its Applications, 482, 27 (2012).
  - [39] H.B. Dang, A.C. Maloof, and M.V. Romalis, *Ultrahigh sensitivity magnetic field and magnetization measurements with an atomic magnetometer*, Appl. Phys. Lett. 97, 151110 (2010).
  - [40] N. Crescini, C. Braggio, G. Carugno, P. Falferi, A. Ortolan, G. Ruoso, *The QUAX-g<sub>p</sub>g<sub>s</sub> experiment to search for monopole-dipole Axion interaction*, Nucl. Instrum. Meth. Phys. Res. A 842, 109 (2017).
  - [41] A. Vinante, M. Bahrami, A. Bassi, O. Usenko, G. Wits, and T.H. Oosterkamp, *Upper Bounds on Spontaneous Wave-Function Collapse Models Using Millikelvin-Cooled Nanocantilevers*, Phys. Rev. Lett. 116, 090402 (2016).
  - [42] A. Vinante, R. Mezzena, P. Falferi, M. Carlesso, and A. Bassi, *Improved Noninterferometric Test of Collapse Models Using Ultracold Cantilevers*, Phys. Rev. Lett. 119, 110401 (2017).
  - [43] Y. B. Zel'dovich, *Generation of Waves by a Rotating Body*, Zh. Eksp. Teor. Fiz. 14, 270 (1971) [JETP Lett. 14, 180 (1971)].
  - [44] J. Schmöle, M. Dragosits, H. Hepach and M. Aspelmeyer, *A micromechanical proof-of-principle experiment for measuring the gravitational force of milligram masses*, Class. Quantum Grav. 33, 12 (2016).
  - [45] S. Bose, A. Mazumdar, G.W. Morley, H. Ulbricht, M. Toroš, M. Paternostro, A.A. Geraci, P.F. Barker, M.S. Kim, and G. Milburn, *Spin Entanglement Witness for Quantum Gravity*, Phys. Rev. Lett. 119, 240401 (2017).
  - [46] C. Marletto and V. Vedral, *Gravitationally Induced Entanglement between Two Massive Particles is Sufficient Evidence of Quantum Effects in Gravity*, Phys. Rev. Lett. 119, 240402 (2017).
  - [47] A.H. Nayfeh and D.T. Mook, *Nonlinear Oscillations*, Wiley Classic Library Classic Edition Published, 1995, pag. 50.
  - [48] L.D. Landau, E.M. Lifshitz, *Electrodynamics of continuous media*, 2nd Edition, Pergamon Press, Oxford, pag. 205.

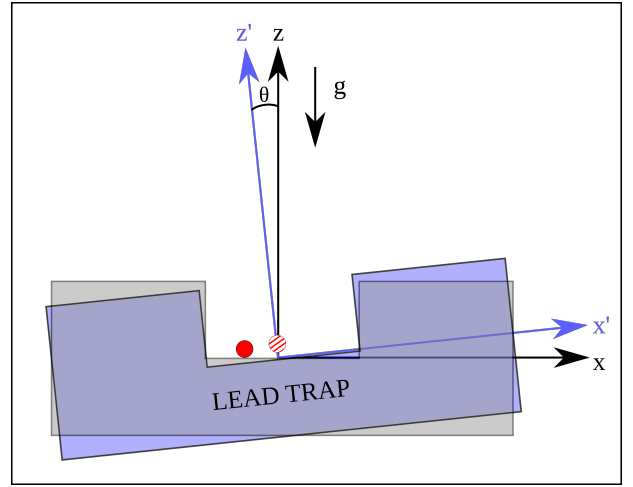


Figure 6: Simplified scheme of the trap with a tilt angle  $\theta$ .

## Appendix A: Numerical study of the System and Frequencies Characterization

The potential energy of a ferromagnetic particle in the presence of a superconductor is described by

$$U = -\frac{1}{2} \int_V d\mathbf{x} \mathbf{M}(\mathbf{x}) \cdot \mathbf{B}_{\text{ind}}(\mathbf{x}) - mgz, \quad (\text{A1})$$

where  $\mathbf{M}$ ,  $m$  and  $V$  are the magnetization, the mass and the volume of the particle, and  $\mathbf{B}_{\text{ind}}$  is the magnetic field induced by the presence of the superconductor. Determining the induced magnetic field for a dynamical system is not an easy task, however as the motion of the magnet is much slower than the time scale of the super-currents and the London penetration depth is much smaller than the characteristic length scale of the system, we can rely on a quasi-static approximation and assume the London penetration depth to be zero. Under this approximation the induced magnetic field  $\mathbf{B}_{\text{ind}}$  can be described by the following differential equation

$$\begin{cases} \nabla \times \mathbf{B}_{\text{ind}} = 0 & x \in \Omega \\ \mathbf{n} \cdot \mathbf{B}_{\text{ind}} = -\mathbf{n} \cdot \mathbf{B}_f & x \in \partial\Omega \end{cases}$$

where  $\partial\Omega$  represents the surface of the superconductor and  $\Omega$  the space outside the superconductor, allowing us to numerically solve the magneto-static problem using a finite-element method with FEniCS software [26].

The simulation was carried out to find the equilibrium positions  $(x_0, y_0, z_0, \beta_0, \alpha_0)$  and the frequencies  $(\omega_x, \omega_y, \omega_z, \omega_\beta, \omega_\alpha)$  in the experimental setup with the  $z$  axis tilted from  $0^\circ$  to  $3^\circ$  with respect to the gravitational axis, as shown in figure 6. We extract the frequencies by fitting the data from the simulation around the minima with a quadratic function. Plots of these frequencies and minima are shown in figure 7.



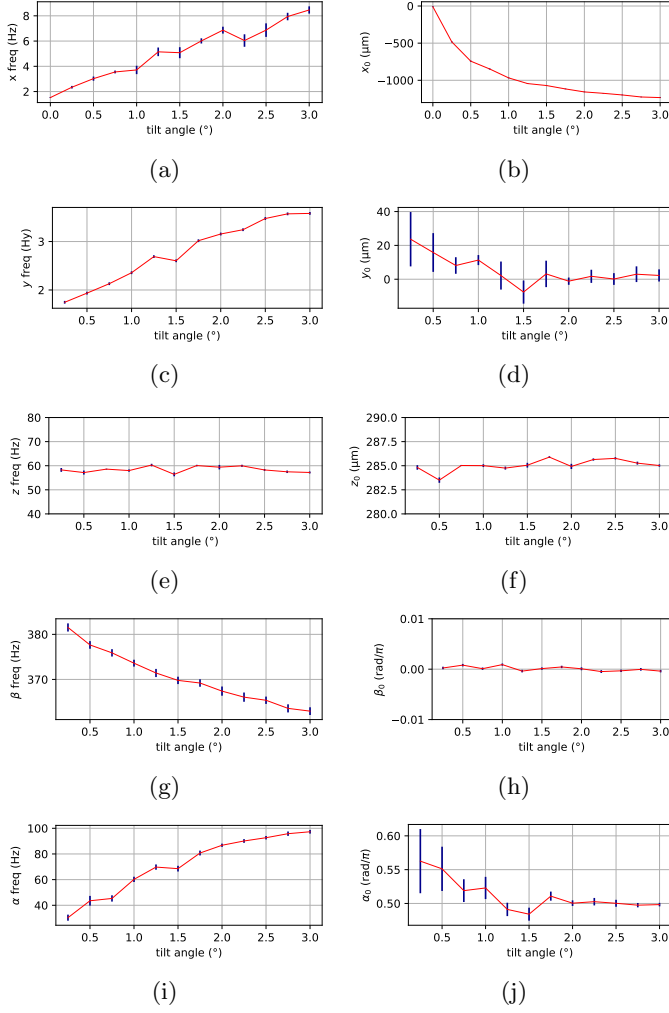


Figure 7: Dependence of the frequencies ( $\omega_x, \omega_y, \omega_z, \omega_\beta, \omega_\alpha$ ) and equilibrium positions ( $x_0, y_0, z_0, \beta_0, \alpha_0$ ) on the angle of tilt ( $\theta$ ) with respect to gravity.

### Appendix B: Calculation of the frequency shift

The frequency shift as a function of the motion amplitude for an unforced mechanical resonator due to nonlinear restoring terms can be calculated using various ways, such as the Lindstedt-Poincare method or the multiple scales method, see for instance ref. [47] for an extensive review.

When the equation of motion is written in the following form, where dissipation terms are neglected and nonlinear terms up to the third order are retained:

$$\ddot{x} + \omega_0^2 x + \alpha_2 x^2 + \alpha_3 x^3 = 0 \quad (\text{B1})$$

the resulting effective resonance frequency is found to be:

$$\tilde{\omega}_0 = \omega_0 \left[ 1 + \left( \frac{3}{8} \frac{\alpha_3}{\omega_0} - \frac{5}{12} \frac{\alpha_2^2}{\omega_0^4} \right) x_A^2 \right] \quad (\text{B2})$$

where  $x_A$  is the amplitude of the oscillation, meaning that the oscillation is written as  $x = x_A \cos(\omega_0 t + \phi_0)$

For the  $\beta$  and  $z$  modes in the present experiment we can start from the potential predicted by the image method model, and Taylor expand up to fourth order. We obtain the following equations of motion:

$$\ddot{z} + \omega_z^2 z - \frac{5}{2} \frac{\omega_z^2}{z_0^2} z^2 + 5 \frac{\omega_z^2}{z_0^3} z^3 = 0 \quad (\text{B3})$$

$$\ddot{\beta} + \omega_\beta^2 \beta - \frac{2}{3} \omega_\beta^2 \beta^3 = 0 \quad (\text{B4})$$

where for each equation we have assumed that only that specific mode is excited at large amplitude, so that cross-coupling terms such as  $\beta^2 z^2$  can be neglected.

Combining Eq. (B2) with Eqs. (B3,B4) we finally obtain:

$$\tilde{\omega}_z = \omega_z \left( 1 - \frac{35}{48} \frac{z_A^2}{z_0^2} \right) \quad (\text{B5})$$

$$\tilde{\omega}_\beta = \omega_\beta \left( 1 - \frac{1}{4} \beta_A^2 \right) \quad (\text{B6})$$

where  $z_A$  and  $\beta_A$  are the oscillation amplitudes. In both cases the nonlinear terms produce a softening effect proportional to the square of the amplitude of oscillation. The frequency shift observed in the experiment can then be used to provide an approximate estimation of the absolute oscillation amplitude.

### Appendix C: Estimation of magnetic dissipation

To estimate dissipation from eddy currents, we assume the microparticle has a finite electrical conductivity  $\sigma$  and relative permeability  $\mu_r \approx 1$ . The latter condition is expected for a hard ferromagnetic particle fully saturated. Under these assumptions the calculation of eddy current losses for a spherical geometry is a standard problem in electromagnetism [48]. Defining the complex polarizability  $\vec{M} = \alpha \vec{H}$ , where  $\vec{M}$  is the magnetization induced by eddy currents and  $\vec{H}$  magnetic field, the induced magnetic moment is  $\vec{\mu}_i = (\alpha' + i\alpha'') V \vec{H}$ . Following Landau-Lifshitz [48] in the low frequency limit  $\delta \gg a$ , where  $\delta = \sqrt{2/\sigma\mu_0\omega}$  is the penetration depth, condition largely fulfilled in our system:

$$\alpha'' = \frac{1}{5} \left( \frac{a}{\delta} \right)^2 \quad (\text{C1})$$

This leads to a power dissipation:

$$W_{ec} = \frac{1}{2\mu_0} \omega \alpha'' B^2 V = \frac{\pi}{15} \sigma \omega^2 a^5 B^2. \quad (\text{C2})$$

where  $V = 4\pi a^3/3$  is the particle volume. The same result can be derived by a direct integration of the power dissipation, under the condition of complete field penetration and dividing the sphere in elementary conductive rings.

In order to calculate the mechanical energy dissipated by eddy currents in the  $\beta$  mode, we note that a rotation of

the magnetic particle by an angle  $\beta$  from the equilibrium position is equivalent to a change of the image magnetic moment  $\Delta\vec{\mu}' = -\mu\beta\hat{z}$ , which produces a change of the  $B$  field orthogonal to  $\vec{\mu}$ :

$$\Delta B = \frac{\mu_0}{4\pi} \frac{\mu\beta}{(2z_0)^3} \quad (\text{C3})$$

For a sinusoidal oscillation of  $\beta$  we can identify  $\Delta B$  with  $B$  in Eq. (C2), and taking into account that the mechanical energy of the mode is  $E = \frac{1}{2}k_\beta\beta^2$  we can finally calculate the loss angle as:

$$\frac{1}{Q_{ec}} = \frac{W_{ec}}{\omega E} \quad (\text{C4})$$

Inserting the parameters of our experiment and assuming a typical value  $\sigma \approx 10^6 \text{ } \Omega^{-1}\text{m}^{-1}$  for NdFeB alloys, we obtain  $Q_{ec} \approx 10^{11}$ . This is clearly too high to explain the measured residual loss.

Magnetic hysteresis losses can be estimated following the same scheme, but now replacing the eddy cur-

rent polarizability with a complex magnetic susceptibility  $\chi = \chi' + i\chi''$ . As we are using a fully saturated hard ferromagnet, we expect  $|\chi| \ll 1$ . The total power dissipation will be given by:

$$W_m = \frac{1}{2\mu_0} \omega \chi'' B^2 V. \quad (\text{C5})$$

and we can calculate  $1/Q_m$  using Eq. (C4) with  $W_m$  in place of  $W_{ec}$ . Carrying out the calculation we find:

$$\frac{1}{Q_m} = \frac{1}{24} \chi'' \left( \frac{a}{z_0} \right)^3 \quad (\text{C6})$$

Assuming that  $\chi''$  is frequency independent and taking into account that  $z_0 \propto a^{\frac{3}{4}}$ , this implies  $1/Q_m \propto a^{\frac{3}{4}}$ , which means that we expect a slightly sublinear increase of  $Q$  when reducing the radius  $a$ . However, if  $\chi'' \propto \omega$  and taking into account that  $\omega_\beta \propto a^{-\frac{5}{8}}$  we find a nearly size-independent behaviour  $1/Q_m \propto a^{\frac{1}{8}}$ .